AGU PUBLICATIONS

Geophysical Research Letters

RESEARCH LETTER
10.1002/2014GL059588

Key Points:
- The Yellowstone magma reservoir is 2.5 times larger than previously thought
- The magma reservoir extends ~15 km NE of the 0.64 Ma caldera boundary
- These results show possible evidence for the NE migration of the hot spot

Supporting Information:
- Readme
- Text S1
- Table S1
- Figure S1
- Figure S2
- Figure S3
- Figure S4
- Figure S5
- Figure S6
- Figure S7
- Figure S8
- Figure S9
- Figure S10

Correspondence to:
J. Farrell,
fishynp@gmail.com

Citation:
Farrell, J., R. B. Smith, S. Husen, and T. Diehl (2014), Tomography from 26 years of seismicity revealing that the spatial extent of the Yellowstone crustal magma reservoir extends well beyond the Yellowstone caldera, *Geophys. Res. Lett.*, *41*, doi:10.1002/2014GL059588.

Received 12 FEB 2014
Accepted 15 APR 2014
Accepted article online 16 APR 2014

Tomography from 26 years of seismicity revealing that the spatial extent of the Yellowstone crustal magma reservoir extends well beyond the Yellowstone caldera

Jamie Farrell[1], Robert B. Smith[1], Stephan Husen[2], and Tobias Diehl[2]

[1]Department of Geology and Geophysics, University of Utah, Salt Lake City, Utah, USA, [2]Swiss Seismological Service, Swiss Federal Institute of Technology, ETH Zurich, Zurich, Switzerland

Abstract The Yellowstone volcanic field has experienced three of Earth's most explosive volcanic eruptions in the last 2.1 Ma. The most recent eruption occurred 0.64 Ma forming the 60 km long Yellowstone caldera. We have compiled earthquake data from the Yellowstone Seismic Network from 1984 to 2011 and tomographically imaged the three-dimensional *P* wave velocity (*Vp*) structure of the Yellowstone volcanic system. The resulting model reveals a large, low *Vp* body, interpreted to be the crustal magma reservoir that has fueled Yellowstone's youthful volcanism. Our imaged magma body is 90 km long, 5–17 km deep, and 2.5 times larger than previously imaged. The magma body extends ~15 km NE of the caldera and correlates with the location of the largest negative gravity anomaly, a −80 mGal gravity low. This new seismic image provides important constraints on the dynamics of the Yellowstone magma system and its potential for future volcanic eruptions and earthquakes.

1. Introduction

The Yellowstone volcanic system is one of the largest silicic volcanic systems in the world and has experienced three major caldera-forming giant volcanic eruptions in the last 2.1 Ma. The most recent giant eruption occurred 0.64 Ma forming the 60 km long Yellowstone caldera [*Christiansen*, 2001]. This episode of explosive volcanism was followed by ~60 smaller rhyolite/basaltic eruptions with the most recent occurring 70,000 years ago. Moreover, Yellowstone exhibits the largest concentration of hydrothermal features in the world [*Christiansen*, 2001] and is characterized by widespread seismicity, unprecedented episodes of ground deformation of uplift and subsidence at rates of up to 7 cm/yr, and extraordinarily high heat flow ~ 2000 m Wm^{-2}. Global tomographic studies show that the youthful Yellowstone volcanic field is fed by a plume that extends from the midmantle to ~50 km depth [*Porritt et al.*, 2014; *Schmandt and Humphreys*, 2010; *Smith et al.*, 2009] which in turn provides basaltic magma that fuels the Yellowstone basaltic/rhyolitic crustal magma reservoir.

Over 45,000 earthquakes have been recorded by the Yellowstone Seismic Network since 1972 with magnitudes ranging $-1.4 \le M_C \le 6.1$ (Figure S1 in the supporting information) making it one of the most seismically active areas in the western U.S. A previous Local Earthquake Tomography (LET) study of the Yellowstone system [*Husen et al.*, 2004] shows low *P* wave velocities beneath the caldera as well as on the NW caldera boundary, but this study as well as earlier LET studies suffered from limited resolution due to the lack of adequate seismic stations and earthquakes in the key areas of Yellowstone during the periods of these studies. Our objective is to employ earthquake data from 1984 to 2011 to tomographically image the Yellowstone crustal velocity structure and to estimate the melt content by incorporating an automatic *P* wave arrival time analysis algorithm combined with three-dimensional seismic tomographic imaging.

2. Earthquake Data Selection

We employed the automatic picking method of *Aldersons* [2004] and *Diehl et al.* [2009a], described in detail in the supporting information, to derive a data set of consistently picked *P* phase first arrival times. To ensure that only the highest-quality data were used for the tomographic inversion, we used earthquakes that have at least eight *P* wave observations, an azimuthal gap of less than 180°, and picks with arrival time uncertainties of less than 0.12 s. The final *P* phase data set consisted of 48,622 high-quality first arrivals from 4520 earthquakes

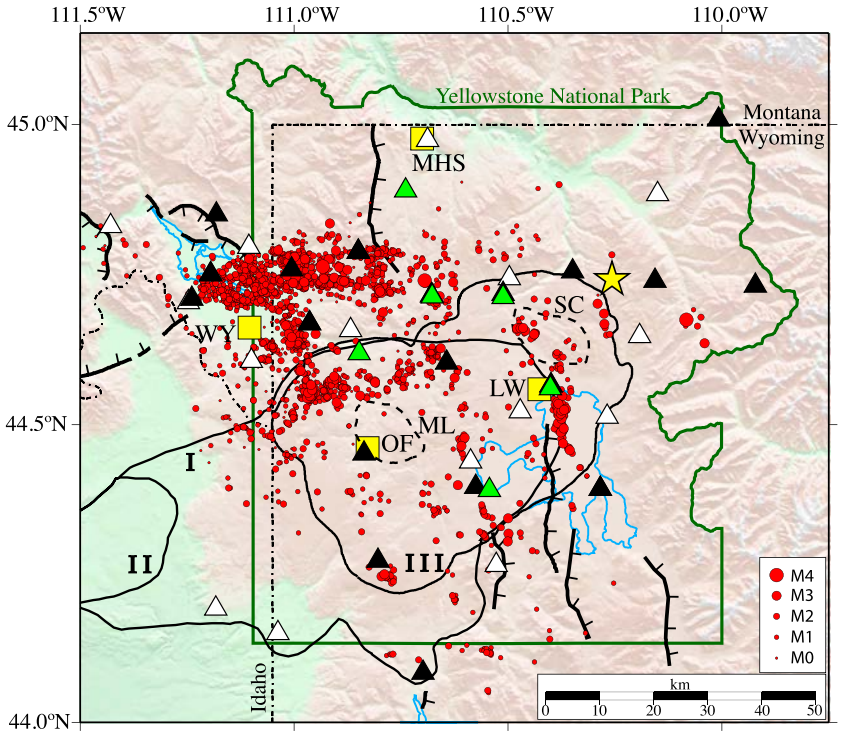

Figure 1. Map of the Yellowstone volcanic field showing the three Late Quaternary calderas and Cenozoic faults. Major faults are shown as bold black lines. Calderas are shown by age: I = 2.1 Ma, II = 1.3 Ma, and III = 0.64 Ma. The youngest caldera is commonly called the Yellowstone caldera. ML and SC represent the Mallard Lake and Sour Creek resurgent domes, which are outlined by dashed lines. Seismic stations of the Yellowstone Seismic Network are shown as black triangles (three-component), green triangles (three-component, borehole), and white triangles (one-component). Yellow squares mark the following: WY = West Yellowstone, Montana; OF = Old Faithful, Wyoming; MHS = Mammoth, Wyoming; and LW = Lake, Wyoming. Red circles indicate earthquakes that were used in the tomographic inversion. Yellow star indicates the location of the Hot Springs Basin Group.

(Figures 1 and S2). The computer code Simulps14 [*Thurber*, 1983; *Eberhart-Phillips*, 1990] was used to invert these data simultaneously for earthquake hypocenters (latitude, longitude, and depths) and origin times as well as the three-dimensional *P* wave velocity structure.

3. Tomographic Solution Quality

Assessing the accuracy of the inverted velocity solution quality is a critical component of seismic tomography. The resulting model resolution mainly depends on the ray coverage (density and geometric distribution of rays), in our case direct and refracted waves from local earthquake sources. The distribution of the derivative weighted sum (DWS) represents the ray path density, and the diagonal element of the resolution matrix (RDE) is sensitive to the geometric distribution of seismic rays [*Diehl et al.*, 2009b]. The combination of RDE with the DWS provides an evaluation of the resulting seismic image and of the quality of the tomographic solution. Overall, the DWS distribution for the tomographic solution is uniform in and around the Yellowstone caldera. In addition the RDE shows very good solution quality in the Yellowstone caldera at 2 and 5 km depths (Figure S3).

To assess the model solution quality and the model's sensitivity to changes in the velocity structure, synthetic sensitivity test results, called checkerboard tests, were performed (Figure S4). To identify and estimate vertical velocity effects on ray paths (leakage), every other layer was perturbed by alternating ±10% *Vp* input anomalies (indicated by blue and red rectangles in Figure S4) and adding in realistic noise levels on the order of our picking uncertainties for each weight class. To identify horizontal smearing (where a model perturbation is artificially spread to multiple grid points), a gap of one grid node between the input anomalies was inserted. The polarities of the input anomalies are swapped for each perturbed layer to distinguish between upward and downward leakage (vertical smearing). The recovery of the input anomalies is excellent for grid nodes in and around the Yellowstone caldera (Figure S4). There was some minor upward leakage into the −4 km

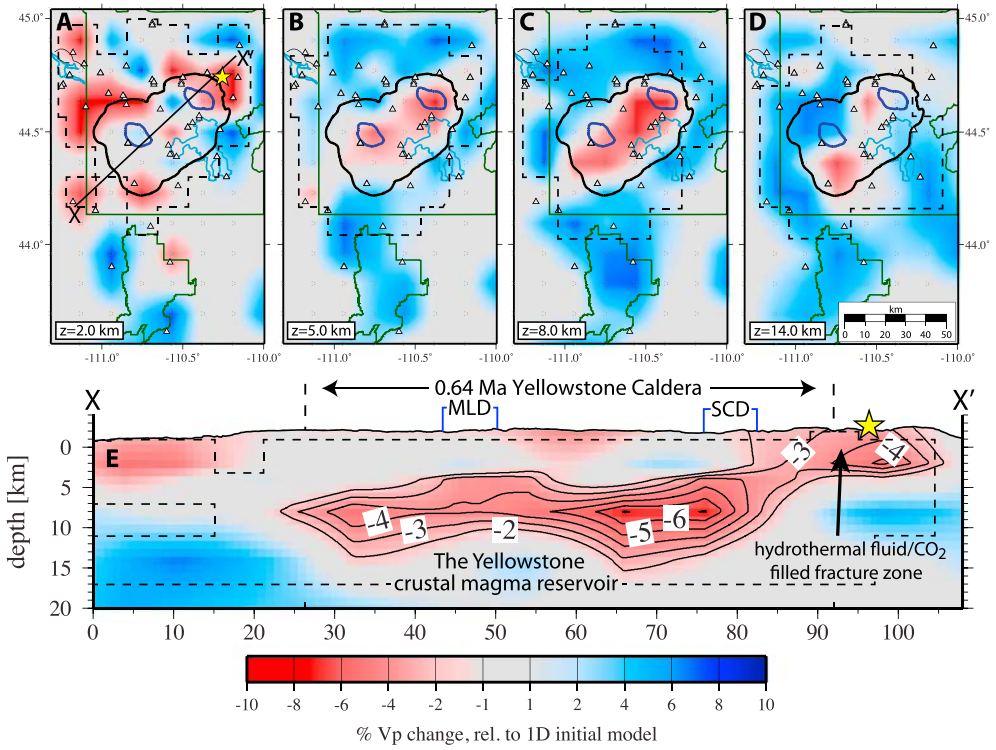

Figure 2. The 3-D *P* wave velocity model for the Yellowstone volcanic system. (a–d) Velocity slices shown at increasing depths and (e) cross section along the long axis of the Yellowstone caldera. Values are in % *Vp* change relative to our minimum 1-D velocity starting model. The solid black line in Figure 2a is the location of the cross section in Figure 2e. White triangles are seismic stations used in the tomographic inversion. The yellow star is the location of the Hot Springs Basin Group. Dashed lines represent the RDE contour of 0.1 and outlines regions of highest resolution.

(relative to sea level) depth layer and downward into the 4 km and 14 km layer with reduced amplitudes and minor horizontal smearing (Figure S4). In the 20 km depth layer, the checkerboard pattern input anomalies are no longer recovered signifying the loss of resolution beneath this depth (Figure S4).

The sensitivity tests shown in Figure S5 were designed to analyze the recovery of the low-velocity bodies beneath and NE of the caldera using the geometry and ray paths of these data. The SW-NE trending cross sections (Figure S5) show the ability of our data to distinguish individual anomalies and to test the depth of resolution with realistic noise levels added. Two separate velocity anomalies with amplitudes of −6% *Vp* (Figures S5a and S5d) and +6% *Vp* (Figure S5b) are shown. These anomalies were well recovered with little vertical or horizontal smearing. In addition, the method was able to recover these anomalies as separate low-velocity bodies. In Figure S5c, a −6% *Vp* anomaly from 5 to 20 km is used as input to test how deep we are able to resolve the velocity changes. Results show that we have adequate resolution down to ~17 km depth. We are not able to resolve changes in the velocity structure below this depth.

4. Yellowstone 3-D *P* Wave Velocity Model and Interpretation

Our final 3-D *Vp* tomographic model achieved a data variance reduction of 60% and a weighted data root-mean-square misfit of 0.13 s, which is of the order of the a priori picking uncertainty. Figure 2 shows the tomographic image of the 3-D *Vp* model at horizontal slices at depths of 2 to 14 km as well as a cross section through the long axis of the Yellowstone caldera. The velocity structure is shown as percentage *Vp* velocity change relative to the 1-D initial reference model that was computed using the reference data set (Table S1). Notably, a low *Vp* body, with *Vp* changes as large as −7%, was imaged below the Yellowstone caldera from ~5 to ~17 km depths. The low-velocity body beneath the caldera extends to even shallower depths (≤5 km), ~15 km NE of the caldera (Figure 2) with *Vp* change values up to −5%. In addition, our model resolves a large, shallow, low *Vp* body located in the northwestern part of the model on the NW boundary of the Yellowstone caldera (Figure 2). This additional low-velocity body has been previously interpreted as a CO_2 saturated gas

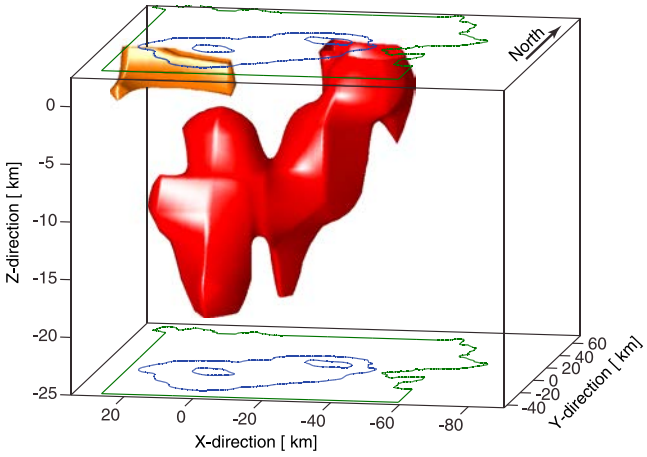

Figure 3. *P* wave velocity isosurface of the Yellowstone crustal magma reservoir. A −2% isosurface of the magma reservoir is shown in red, and a −6% isosurface of the low *Vp* body that was previously interpreted as a CO_2 gas-saturated volume is shown in orange. Blue lines outline the 0.64 Ma Yellowstone caldera and the two resurgent domes.

body based on low *Vp* and low *Vp/Vs* ratios [*Husen et al.*, 2004]. We conducted extensive resolution and sensitivity analyses to test the ability of our model and data to recover velocity changes for this study, and these are described in detail in the supporting information.

A −2% *P* wave velocity isosurface of the Yellowstone magma reservoir and surrounding hot material (red) and a −6% *Vp* isosurface of the low-velocity body on the NW caldera boundary (orange) are shown in Figure 3. If we assume that only the strongest anomalies (≥4% *Vp* change) contain partial melt with a conservative estimate of melt fraction of 5–15% (given *P* wave velocities of ~4.8 to 5.4 km/s) (Figure S6) [*Chu et al.*, 2010], we estimate the volume of melt to be 200 km^3 to 600 km^3. This melt fraction is significantly smaller than a previously determined value of 32% based on teleseismic receiver function analysis that employed 570 earthquakes recorded on five broadband seismic stations [*Chu et al.*, 2010].

Our new estimate of the Yellowstone magma reservoir volume is 2.5 times larger than the previous tomographic determination [*Husen et al.*, 2004]. In comparison, it is estimated that the three Yellowstone giant eruptions 2.1, 1.3, and 0.64 Ma ago erupted 2500 km^3, 280 km^3, and 1000 km^3 of material, respectively [*Christiansen*, 2001]. Based on our estimates of the Yellowstone magma reservoir, there is thus sufficient melt volume for another similar sized eruption as the 1.3 Ma eruption. However, we cannot robustly estimate the porosity distribution using seismic tomography. It remains unclear how lateral variations in porosity, permeability, temperature, and rheology would affect the system's ability to produce a unified eruption. In addition, the calculation of the melt fraction is extremely simple and other factors, e.g., temperature or rheological variations, could affect the results.

An unexpected finding of our study is that a continuity of low *P* wave velocities ~15 km NE of the Yellowstone caldera coincides with the largest negative Bouguer gravity anomaly, −80 mGal, in the Yellowstone Plateau (Figure S7a). Previous gravity modeling [*DeNosaquo et al.*, 2009] revealed that the lowest density material extends ~20 km NE of the caldera (Figure S7b), similar to our *Vp* model, although our imaged anomaly is shallower than the low-density anomaly NE of the Yellowstone caldera (Figure S7b). Importantly, the distance the Yellowstone hot spot would "migrate" due to the SW motion of the North American plate, at ~2.35 cm/yr [*Anders et al.*, 2014], since the last major Yellowstone eruption at 0.64 Ma shows an apparent NE migration of ~15 km which again is strikingly similar to the NE extent of the low-velocity body imaged in this study. This suggests that the apparent NE migration of the Yellowstone hot spot over the last 640,000 years has fueled the crustal magma reservoir through new magma pathways NE of the caldera. Note that the imaged shallow low-velocity anomaly NE of the caldera is at the extent of our resolution so it is possible that it extends farther to the NE.

In addition, the shallowest portion of the Yellowstone magma reservoir underlies the large Hot Spring Basin Group (HSB) (yellow star in Figures 1, 2, 4, and S7) northeast of the caldera, the largest area of hydrothermal alteration and one of the most thermally active basins in Yellowstone [*DeNosaquo et al.*, 2009; *Werner et al.*, 2008]. Gas geothermometer temperatures of HSB approach 300°C and suggest that the hydrothermal reservoir fueling the thermal state of the HSB is one of the hottest at Yellowstone [*Werner et al.*, 2008]. The high temperature of HSB and our tomographic results thus support the idea that the northeastern region of the Yellowstone caldera hosts a highly fractured fluid-filled upper crustal volume overlying the shallowest portion of the Yellowstone crustal magma reservoir [*Werner et al.*, 2008]. An alternate interpretation is that the low-velocity body beneath the HSB may represent an area where magmatic fluids (gas, hydrothermal

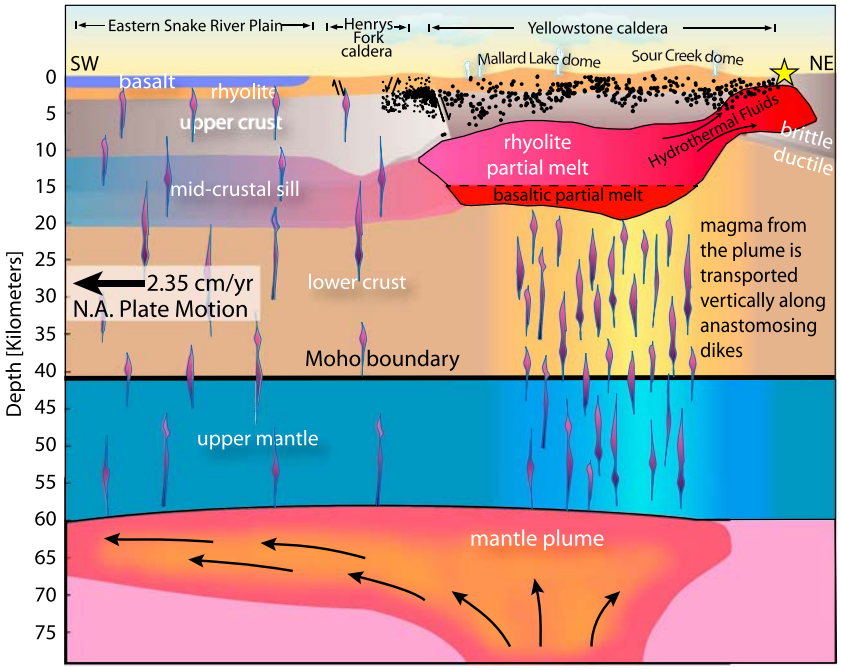

Figure 4. Plume-plate interaction model for the Yellowstone hot spot and the evolution of the Yellowstone-Snake River Plain volcano system. The model derived from this study shows how basaltic melt from the plume rises buoyantly through the upper mantle and lower crust, partially melting the silicic continental crust and creating a partially melted magma reservoir beneath Yellowstone and well beyond the caldera. This energetic magmatic system drives Yellowstone's hydrothermal system, extraordinary high heat flow, and seismicity. As the lithosphere passes over the plume the plate cools and thermally contracts above the crystallizing fractionated crustal magma reservoir forming the characteristic bimodal rhyolite-basalt volcanic system of the Yellowstone-Snake River Plain [after *DeNosaquo et al.*, 2009].

fluids, and melt) have migrated to shallower depths away from the magma reservoir along existing fractures. This idea is supported by the fact that the shallow low-velocity body to the NE of the caldera is clearly connected to the main body of the magma reservoir beneath the Yellowstone caldera.

While there have been many studies to determine the velocity structure beneath volcanoes using seismic tomography and many exhibit low-velocity bodies that are interpreted as magma reservoirs at shallow depths, the newly imaged Yellowstone crustal magma reservoir is the largest we know of. For example, seismic tomographic studies of the Long Valley caldera, California, revealed low *Vp* bodies at depths of 6 km and 8–14 km beneath the caldera and are interpreted to reflect the ascent path of magmatic fluids into the upper crust [*Seccia et al.*, 2011]. In addition, the Toba Volcano, Indonesia, considered the world's largest active volcano, shows two separate low *Vp* bodies in the upper 10 km separated by a zone of locally high velocities, indicating that the shallow, subcaldera magma system is composed of two separate reservoirs [*Masturyono et al.*, 2001]. Thus, the Yellowstone crustal magma reservoir is, to date, the largest tomographically imaged active magma reservoir in the world.

These new results could provide new insights on the eruptive capability of the Yellowstone volcanic system and bear on the physics of magma recharge and migration. Our findings are important to the results of recent studies [*Malfait et al.*, 2014; *Caricchi et al.*, 2014] that show that large silicic caldera systems and their associated magma reservoirs can produce supereruptions that are triggered solely by magma buoyancy that may well be the case for Yellowstone.

5. Conclusions

The Yellowstone crustal magma reservoir is an integral part of the larger Yellowstone volcanic field (Figure 4) in which a fixed Yellowstone mantle plume feeds buoyant transport of basaltic melt and heat from mantle depths into the crust beneath Yellowstone National Park creating the magma reservoir that we image here. Our estimates suggest that the Yellowstone crustal magma reservoir contains partially molten material

(5–15 % partial melt) that is considered a working model for the source of the caldera-forming dominantly rhyolitic eruptions of Yellowstone and the bimodal basaltic-rhyolitic volcanism of the Snake River Plain volcanic field. Importantly, many of the extensive earthquake swarms in Yellowstone [*Farrell et al.*, 2010; *Massin et al.*, 2013; *Shelly et al.*, 2013] are attributed to migrating magmatic fluids from the Yellowstone crustal magma reservoir that results in a much larger earthquake source capability than from caldera magmatism alone. Overall, this new image of Yellowstone's crustal magma reservoir provides a better understanding of the magmatic volume, melt configuration, and fluid state that control its potential for future volcanism and its joint volcano-earthquake hazard, as well as a basis for assessing temporal changes in the reservoir properties that could portend new volcanism. We specifically note that assessments of Yellowstone volcano hazard [*Christiansen et al.*, 2007] will not appreciably change with our new findings because the Yellowstone Late Quaternary volcanic history has been well defined in terms of ages, sizes, and frequency of eruptions that capture the record of the entire large magma body imaged here.

Acknowledgments

Data employed in this study were from the archives of the University of Utah Seismograph Stations, which operates and archives data from the Yellowstone Seismic Network. Funding for the study was primarily from The Brinson Foundation, the Carrico funds, and the University of Utah. We appreciate the critical reviews by Keith Koper, David Hill, Michele Paulatto, and an anonymous reviewer.

The Editor thanks Michele Paulatto and an anonymous reviewer for their assistance in evaluating this paper.

References

Aldersons, F. (2004), Toward three-dimensional crustal structure of the Dead Sea region from local earthquake tomography, PhD thesis, Tel Aviv University, Israel.

Anders, M. H., D. W. Rodgers, S. R. Hemming, J. Saltzman, V. J. DiVinere, J. T. Hagstrum, G. F. Embree, and R. C. Walter (2014), A fixed sub-lithospheric source for the late Neogene track of the Yellowstone hotspot: Implications of the Heise and Picabo Volcanic Fields, *J. Geophys. Res. Solid Earth*, *119*, doi:10.1002/2013JB010483.

Caricchi, L., C. Annen, J. Blundy, G. Simpson, and V. Pinel (2014), Frequency and magnitude of volcanic eruptions controlled by magma injection and buoyancy, *Nat. Geosci.*, *7*, 126–130, doi:10.1038/NGEO2041.

Christiansen, R. L. (2001), The Quaternary and Pliocene Yellowstone plateau volcanic field of Wyoming, Idaho, and Montana, *U.S. Geol. Surv. Prof. Pap.*, *729-G*, 145.

Christiansen, R. L., J. B. Lowenstern, R. B. Smith, H. Heasler, L. A. Morgan, M. Nathenson, L. G. Mastin, L. J. P. Muffler, and J. E. Robinson (2007), Preliminary assessment of volcanic and hydrothermal hazards in Yellowstone National Park and vicinity, *U.S. Geol. Surv. Open File Rep., 2007–1071*, 94 pp.

Chu, R., D. V. Helmberger, D. Sun, J. M. Jackson, and L. Zhu (2010), Mushy magma beneath Yellowstone, *Geophys. Res. Lett.*, *37*, L01306, doi:10.1029/2009GL041656.

DeNosaquo, K., R. B. Smith, and A. R. Lowry (2009), Density and lithospheric strength models of the Yellowstone-Snake River Plain volcanic system from gravity and heat flow data, *J. Volcanol. Geotherm. Res.*, *188*, 108–127.

Diehl, T. E., E. Kissling, S. Husen, and F. Aldersons (2009a), Consistent phase picking for regional tomography models: Application to the greater Alpine region, *Geophys. J. Int.*, *176*, 542–554.

Diehl, T., S. Husen, E. Kissling, and N. Deichmann (2009b), High-resolution 3-D *P*-wave model of the Alpine crust, *Geophys. J. Int.*, *179*, 1133–1147.

Eberhart-Phillips, D. (1990), Three-dimensional *P* and *S* velocity structure in the Coalinga region, California, *J. Geophys. Res.*, *95*, 15,343–15,363, doi:10.1029/JB095iB10p15343.

Farrell, J., R. B. Smith, T. Taira, W.-L. Chang, and C. M. Puskas (2010), Dynamics and rapid migration of the energetic 2008–2009 Yellowstone Lake earthquake swarm, *Geophys. Res. Lett.*, *37*, L19305, doi:10.1029/2010GL044605.

Husen, S., R. B. Smith, and G. P. Waite (2004), Evidence for gas and magmatic sources beneath the Yellowstone volcanic field from seismic tomographic imaging, *J. Volcanol. Geotherm. Res.*, *131*, 397–410.

Malfait, W. J., R. Seifert, S. Petitgirard, J.-P. Perrillat, M. Mezouar, T. Ota, E. Nakamura, P. Lerch, and C. Sanchez-Valle (2014), Supervolcano eruptions driven by melt buoyancy in large silicic magma chambers, *Nat. Geosci.*, *7*, 122–125, doi:10.1038/NGEO2042.

Massin, F., J. Farrell, and R. B. Smith (2013), Repeating earthquakes in the Yellowstone volcanic field: Implications for rupture dynamics, ground deformation, and migration in earthquake swarms, *J. Volcanol. Geotherm. Res.*, *257*, 159–173.

Masturyono, R. McCaffrey, D. A. Wark, S. W. Roecker, F. Ibrahim, G. Ibrahim, and Sukhyar (2001), Distribution of magma beneath the Toba caldera complex, north Sumatra, Indonesia, constrained by three-dimensional *P* wave velocities, seismicity, and gravity data, *Geochem. Geophys. Geosyst.*, *2*, 1014, doi:10.1029/2000GC000096.

Porritt, R. W., R. M. Allen, and F. F. Pollitz (2014), Seismic imaging east of the Rocky Mountains with USArray, *Earth Planet. Sci. Lett.*, doi:10.1016/j.epsl.2013.10.034, in press.

Schmandt, B., and E. Humphreys (2010), Complex subduction and small-scale convection revealed by body-wave tomography of the western United States upper mantle, *Earth Planet. Sci. Lett.*, *297*, 435–445.

Seccia, D., C. Chiarabba, and P. De Gori, I. Bianchi, and D. P. Hill (2011), Evidence for the contemporary magmatic system beneath Long Valley Caldera from local earthquake tomography and receiver function analysis, *J. Geophys. Res.*, *116*, B12314, doi:10.1029/2011JB008471.

Shelly, D. R., D. Hill, F. Massin, J. Farrell, R. B. Smith, and T. Taira (2013), A fluid-driven earthquake swarm on the margin of the Yellowstone caldera, *J. Geophys. Res. Solid Earth*, *118*, 1–15, doi:10.1002/jgrb.50362.

Smith, R. B., M. Jordan, B. Steinberger, C. M. Puskas, J. Farrell, G. P. Waite, S. Husen, W.-L. Chang, and R. O'Connell (2009), Geodynamics of the Yellowstone hotspot and mantle plume: Seismic and GPS imaging, kinematics, and mantle flow, *J. Volcanol. Geotherm. Res.*, *188*, 26–56.

Thurber, C. H. (1983), Earthquake locations and three-dimensional crustal structure in the Coyote Lake area, central California, *J. Geophys. Res.*, *88*, 8226–8236, doi:10.1029/JB088iB10p08226.

Werner, C., S. Hurwitz, W. C. Evans, J. B. Lowenstern, D. Bergfeld, H. Heasler, C. Jaworowski, and A. Hunt (2008), Volatile emissions and gas geochemistry of Hot Springs Basin, Yellowstone National Park, USA, *J. Volcanol. Geotherm. Res.*, *178*, 751–762.

Auxiliary Material for

Tomography from twenty-six years of seismicity reveals the spatial extent of the Yellowstone crustal magma reservoir extends well beyond the Yellowstone caldera.

Jamie Farrell[1], Robert B. Smith[1], Stephan Husen[2], Tobias Diehl[2]

([1] University of Utah Dept. of Geology and Geophysics, Salt Lake City, UT 84112. [2]Swiss Seismological Service, Swiss Federal Institute of Technology, ETH Zurich, CH-8092, Switzerland.)

Geophysical Research Letters, 2014

Introduction

This supplemental section contains a description of the automatic picking algorithm that was used in the analysis for this paper and the process used to select the data used in the tomographic inversion. In addition, this section contains several figures that could not fit in the main body of the paper but is important in the description of the data analysis and background of the study.

Figure S1 – Map of Yellowstone earthquakes, 1973 to 2013, relocated with the new 3D velocity model developed in this study. Epicenters are shown as red dots, and faults are shown as thin black lines. The outline of the 0.64 Ma Yellowstone caldera

is shown in black and the two volcanic resurgent domes are outlined as black dotted lines. Hydrothermal areas are shown in green.

Figure S2 – Map of earthquakes from which digital P-wave waveform data were used for the final, high-quality dataset (red circles). Gray lines represent seismic ray paths connecting stations (black triangles) and epicenters. Black line outlines the Yellowstone caldera.

Figure S3 – Derivative Weight Sum (DWS) values for various depths that are assumed to be a proxy for ray density (top row). Diagonal elements of the resolution matrix (RDE) of the *Vp* solution are shown at various depths (bottom row).

Figure S4 – Checkerboard velocity model sensitivity test. Recovered model after 2 iterations is shown in plane view at different depths. Alternating ±10% input anomalies are indicated by blue and red squares, respectively at A) 2, 8, and 20 km and B) -4, 4, and 14 km. Dashed lines represent the RDE contour of 0.1 and outlines regions of highest resolution.

Figure S5 – Assessment of solution quality in the region of the Yellowstone crustal magma reservoir using synthetic characteristic models: (A) Input model of -6% (red boxes), (B) input model of +6% (blue boxes), (C) deep input model of -6% (red box), and (D) larger input model of -6% (red boxes). Dashed lines represent the RDE contour of 0.1 and outlines regions of highest resolution. Cross section location shown in Figure 2.

Figure S6 – Porosity (% partial melt) versus P-wave velocity. Our results, bracketed in red, show velocities in the Yellowstone magma reservoir from ~4.8 to

5.4 km/s which corresponds to porosities from ~5 to 15% shown by the solid and dashed red lines, modified from Chu et al. [2010].

Figure S7 – Bouguer Gravity map and corresponding density model of Yellowstone. The lowest density body extends ~20 km beyond the northeastern edge of the caldera [DeNosaquo et al., 2009]. (A) Bouguer Gravity map of the Yellowstone region. Densities are in kg/m. Red stippled body is the approximate outline of the seismic low-velocity body determined in this study. The blue stippled body outlines the seismic low-velocity body of the earlier study of Husen et al. [2004]. The steep gravity gradient, NE of the caldera, indicates that the body responsible for the large negative gravity anomaly is shallower NE of the caldera corresponding to the location of shallowest low-velocity body. The yellow star indicates the location of the Hot Springs Basin Group. (B) Cross section showing the density model [DeNosaquo et al., 2009] and the low *Vp* body (red stippled body) imaged in this study.

Figure S8 – Performance of the automated picking algorithm, MPX, for a weighting scheme derived from reference events in group A and applied to both group A and B. The *Nij* denote the number of picks of reference class *i* classified by MPX as automatic class *j*. The *σij* represent the standard deviation for differences between reference picks of class *i* and corresponding automatic picks of class *j*. ε represents the uncertainty assigned to the corresponding reference weight. White bars indicate correct classification, gray bars indicate downgrading, and black bars identify upgrading of picks by the automated algorithm. The automatic weighting classifies more than 60% of the class '0' picks correctly.

Figure S9 – Same as Figure S8 except using reference events in group A and applied to both group A and B with stations with |res|>1 removed.

Figure S10 – Residual distribution of weight classes located using the automated picking algorithm picks after stations with initial |residuals|>1.0 s removed.

Table S1 - Initial P-wave velocities at nodes of the 3-D gradient model. Velocities are based on the calculated minimum 1-D model.

Supplemental Material

Automatic P-wave Arrival Time Analysis Algorithm: The automatic picking algorithm, MPX, employed here automates the determination of the first P-wave arrival time of a seismic signal [Aldersons, 2004; Diehl et al. 2009]. This algorithm requires an initial pick to guide the analysis to an approximate P-phase onset time. The initial picks in this study are provided by predicted P-wave arrival times using the derived minimum 1-D velocity model and station corrections. Note the term "pick", commonly used by seismologists, defines the onset time of an observed seismic phase on a seismogram. The uncertainty of arrival time picks in our dataset is estimated to be ≤ 0.12 sec.

The MPX picking system combines the Baer-Kradolfer algorithm [Baer & Kradolfer, 1987] with an automated pick-quality assessment. The threshold for the Baer-Kradolfer picker is derived adaptively by comparing seismic noise and signal characteristics. A noise window and a signal window are centered on the initial pick and are separated by "safety gaps". Safety gap lengths depend on the expected difference between the predicted arrival time and the actual phase onset. The larger the safety gap, the higher probability there is for incorrect arrival time determinations [Diehl, 2008].

A pattern recognition scheme weights different waveform attributes (predictors) obtained in the time window around the predicted arrival time and classifies the automatic arrival time in discrete quality classes. The corresponding weighting factors are the statistical 'Fisher coefficients', which have to be calibrated with a set of reference manual picks (reference data). A multiple discriminant analysis (MDA) is used to derive appropriate Fisher coefficients from the reference picks.

326 The reference set of manually analyzed arrival times from 171 earthquakes (3,189 P-
327 picks) was divided in half into groups A and B. Group A was used to derive appropriate
328 Fisher coefficients for automatic quality classification. The MDA algorithm compares
329 the predictor values around the automatic arrival time with the associated reference
330 quality class. The derived Fisher coefficients are considered to represent the optimum
331 weighting of each predictor to estimate the corresponding quality class membership
332 [Diehl et al., 2009]. The Fisher coefficients derived using group A were then input into
333 MPX for automatic picking on the entire reference dataset. This allows us to test how
334 well the Fisher coefficients derived for group A are applied (in MPX) to both groups A
335 and B.

336 Figure S8 illustrates the performance of the weighting scheme determination in terms of
337 accuracy and classification of assigned weight class when applied to all reference events.
338 N_{ij} denotes the number of picks of reference class i classified by the pattern recognition
339 scheme as automatic class j. The σ_{ij} value represents the standard deviation for
340 differences between reference picks of class i and corresponding automatic picks of class
341 j. A satisfactory automatic picking and quality assessment is achieved if the deviation
342 between automatic and reference picks is within the error interval of automatic quality
343 classification ($\sigma_{ij} \leq \varepsilon_j$) and if only few low quality reference picks are moderately
344 upgraded to higher quality classes by MPX.

345 However, upgrades from lowest to highest quality classes lead to a distortion of the data
346 error estimates in the resultant tomographic model and could generate artifacts in
347 tomographic images [Diehl et al., 2009]. Inspection of Figure S8 shows that a number of
348 reference class 4 (rejected) and reference class 3 events were upgraded to automatic class

0 and 1 weights, which is unacceptable for use in tomographic inversions as it could introduce large artifacts in the derived velocity model. Inspection of these data show that the majority of these arrival times were associated with either bad waveform data (spikes, etc.) that MPX picked on or waveforms where MPX picked a later, more impulsive arrival, instead of the first-arriving emergent phase.

To remove these erroneous picks and bad data files, we employed the following algorithm:

1. Only use earthquakes with picks from at least 8 seismic stations (nobs $\geq$ 8) and an azimuthal gap between raypaths less than 180º from initial locations using the minimum 1-D velocity model.
2. Run MPX algorithm using Fisher coefficients derived from reference group A to calculate automatic picks.
3. Relocate the events using automatic picks and the minimum 1-D velocity model.
4. Remove data from any station with a residual greater than 1.0 second or less than -1 second (|res| > 1 s).
5. Re-run MPX algorithm using the filtered data to generate automatic picks of the remaining high-quality data.

Figure S9 shows the results of using the algorithm described above. Using only well-located events and removing data from stations with |residuals| > 1.0 s successfully removed the majority of the bad waveforms and mispicks. Results show that there are no longer any picks that were upgraded from reference weight 4 to automatic weights 0 and

1. Also, reference weight 3 picks that were upgraded to automatic weight 0 picks have also been removed. However, there remains a relatively large number of reference-weight 4 picks (32 in total) updated to automatic-weight 2. In addition, analyzing the station residuals after re-locating the events using the automatic picks, allows us to inspect the quality of our picks. Weights 0 and 1 show well-behaved (Gaussian) distributions (Fig. S10). However, weights 2 and 3 show less desirable distributions with uneven tails and bi-modal distributions. Because of this, we only accept automatic weights 0 and 1 picks for use in the tomographic inversion.

Figures:

Fig. S1 – Map of Yellowstone earthquakes, 1973 to 2013, relocated with the new 3D velocity model developed in this study. Epicenters are shown as red dots, and faults are shown as thin black lines. The outline of the 0.64 Ma Yellowstone caldera is shown in black and the two volcanic resurgent domes are outlined as black dotted lines. Hydrothermal areas are shown in green.

Fig. S2 – Map of earthquakes from which digital P-wave waveform data were used for the final, high-quality dataset (red circles). Gray lines represent seismic ray paths connecting stations (black triangles) and epicenters. Black line outlines the Yellowstone caldera.

Fig. S3 - Derivative Weight Sum (DWS) values for various depths that are assumed to be a proxy for ray density (top row). Diagonal elements of the resolution matrix (RDE) of the *Vp* solution are shown at various depths (bottom row).

Fig. S4 - Checkerboard velocity model sensitivity test. Recovered model after 2 iterations is shown in plane view at different depths. Alternating ±10% input anomalies are indicated by blue and red squares, respectively at A) 2, 8, and 20 km and B) -4, 4, and 14 km. Dashed lines represent the RDE contour of 0.1 and outlines regions of highest resolution.

Fig. S5 – Assessment of solution quality in the region of the Yellowstone crustal magma reservoir using synthetic characteristic models: (A) Input model of -6% (red boxes), (B) input model of +6% (blue boxes), (C) deep input model of -6% (red box), and (D) larger input model of -6% (red boxes). Dashed lines represent the RDE contour of 0.1 and outlines regions of highest resolution. Cross section location shown in Figure 2.

Fig. S6 – Porosity (% partial melt) versus P-wave velocity. Our results, bracketed in red, show velocities in the Yellowstone magma reservoir from ~4.8 to 5.4 km/s which corresponds to porosities from ~5 to 15% shown by the solid and dashed red lines, modified from Chu et al. [2010].

Fig. S7 – Bouguer Gravity map and corresponding density model of Yellowstone. The lowest density body extends ~20 km beyond the northeastern edge of the caldera [DeNosaquo et al., 2009]. (A) Bouguer Gravity map of the Yellowstone region. Densities are in kg/m. Red stippled body is the approximate outline of the seismic low-velocity body determined in this study. The blue stippled body outlines the seismic low-velocity body of the earlier study of Husen et al. [2004]. The steep gravity gradient, NE of the caldera, indicates that the body responsible for the large negative gravity anomaly is shallower NE of the caldera

corresponding to the location of shallowest low-velocity body. The yellow star indicates the location of the Hot Springs Basin Group. (B) Cross section showing the density model [DeNosaquo et al., 2009] and the low *Vp* body (red stippled body) imaged in this study.

Fig. S8 - Performance of the automated picking algorithm, MPX, for a weighting scheme derived from reference events in group A and applied to both group A and B. The *Nij* denote the number of picks of reference class *i* classified by MPX as automatic class *j*. The *σij* represent the standard deviation for differences between reference picks of class *i* and corresponding automatic picks of class *j*. ε represents the uncertainty assigned to the corresponding reference weight. White bars indicate correct classification, gray bars indicate downgrading, and black bars identify upgrading of picks by the automated algorithm. The automatic weighting classifies more than 60% of the class '0' picks correctly.

Fig. S9 – Same as Figure S8 except using reference events in group A and applied to both group A and B with stations with |res|>1 removed.

Fig. S10 - Residual distribution of weight classes located using the automated picking algorithm picks after stations with initial |residuals|>1.0 s removed.

Tables:

Table. S1 – Initial P-wave velocities at nodes of the 3-D gradient model. Velocities are based on the calculated minimum 1-D model.

Table S1. Initial P-wave velocities at nodes of the 3-D gradient model. Velocities are based on the calculated minimum 1-D model.

Depth of grid plane (km)	*Vp* (km/s)
-10	3.70
-4	3.80
2	5.24
4	5.42
8	5.65
14	6.12
20	6.30
50	6.50

Fig. S01

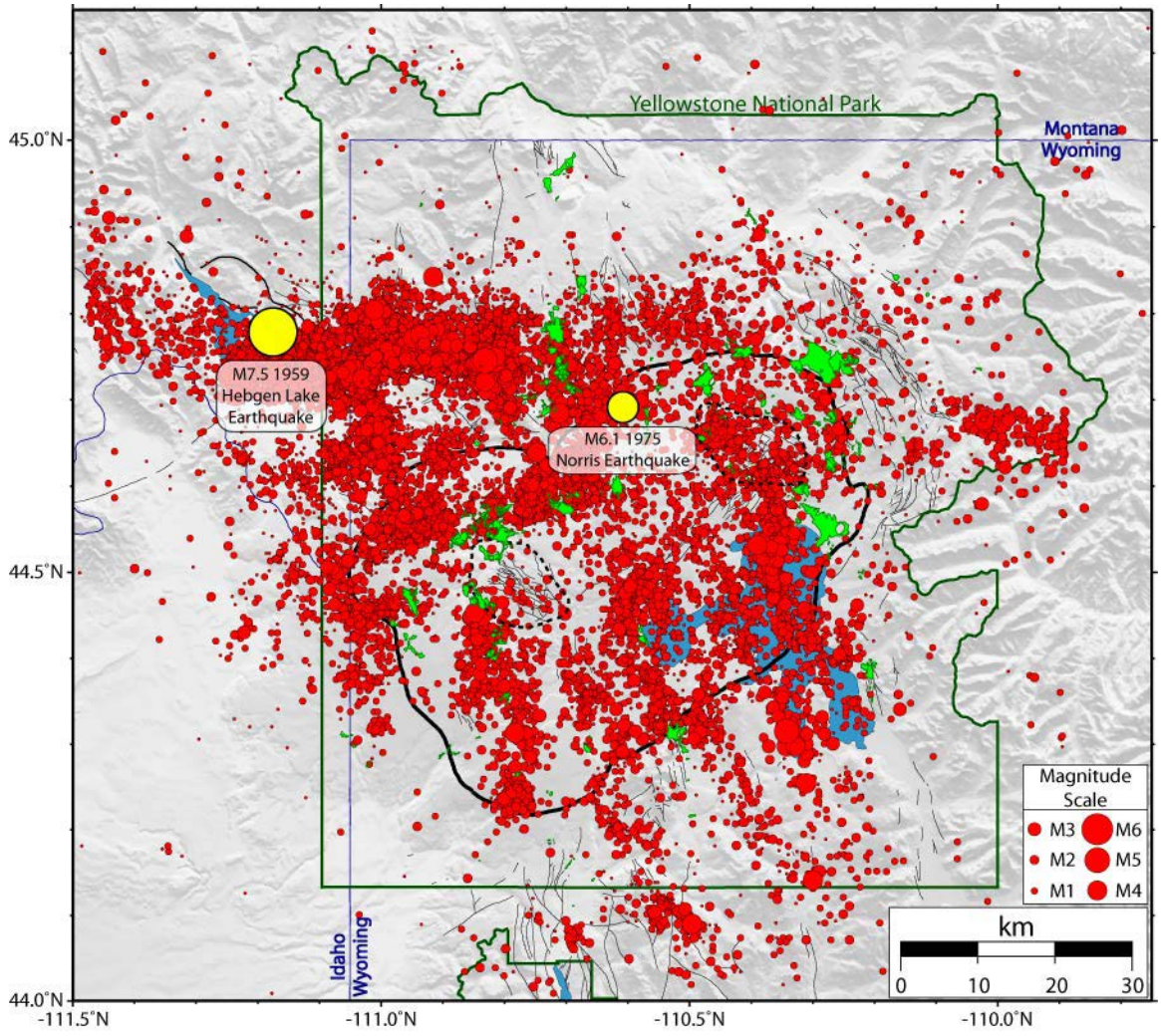
Yellowstone National Park
Montana
Wyoming
M7.5 1959
Hebgen Lake
Earthquake
M6.1 1975
Norris Earthquake
Idaho
Wyoming
Magnitude
Scale
M3
M6
M2
M5
M1
M4
km
0
10
20
30
45.0°N
44.5°N
44.0°N
-111.5°N
-111.0°N
-110.5°N
-110.0°N

Fig. S02

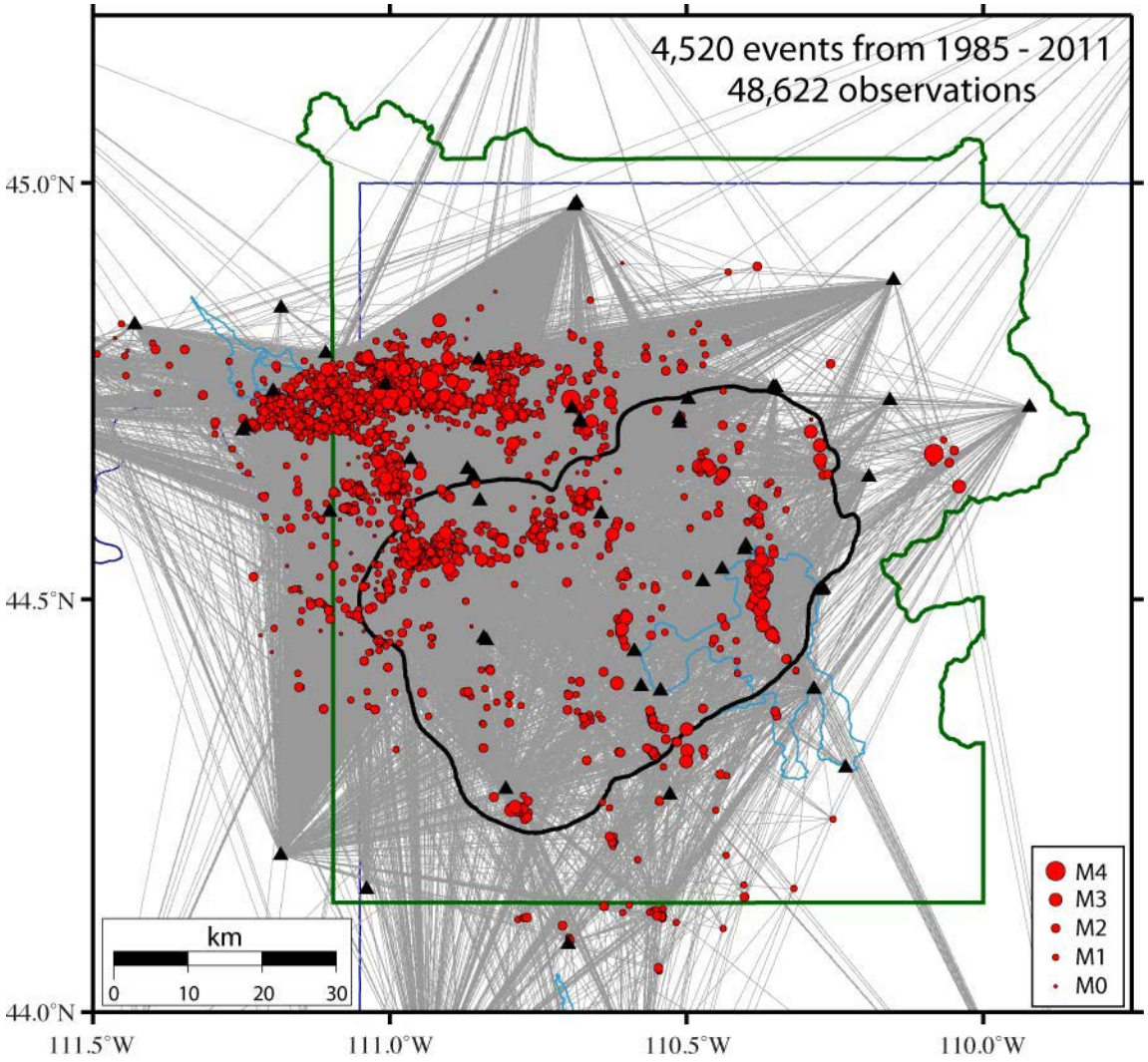
4,520 events from 1985 - 2011
48,622 observations
45.0°N
44.5°N
44.0°N
111.5°W
111.0°W
110.5°W
110.0°W
km
0
10
20
30
M4
M3
M2
M1
M0

Fig. S03

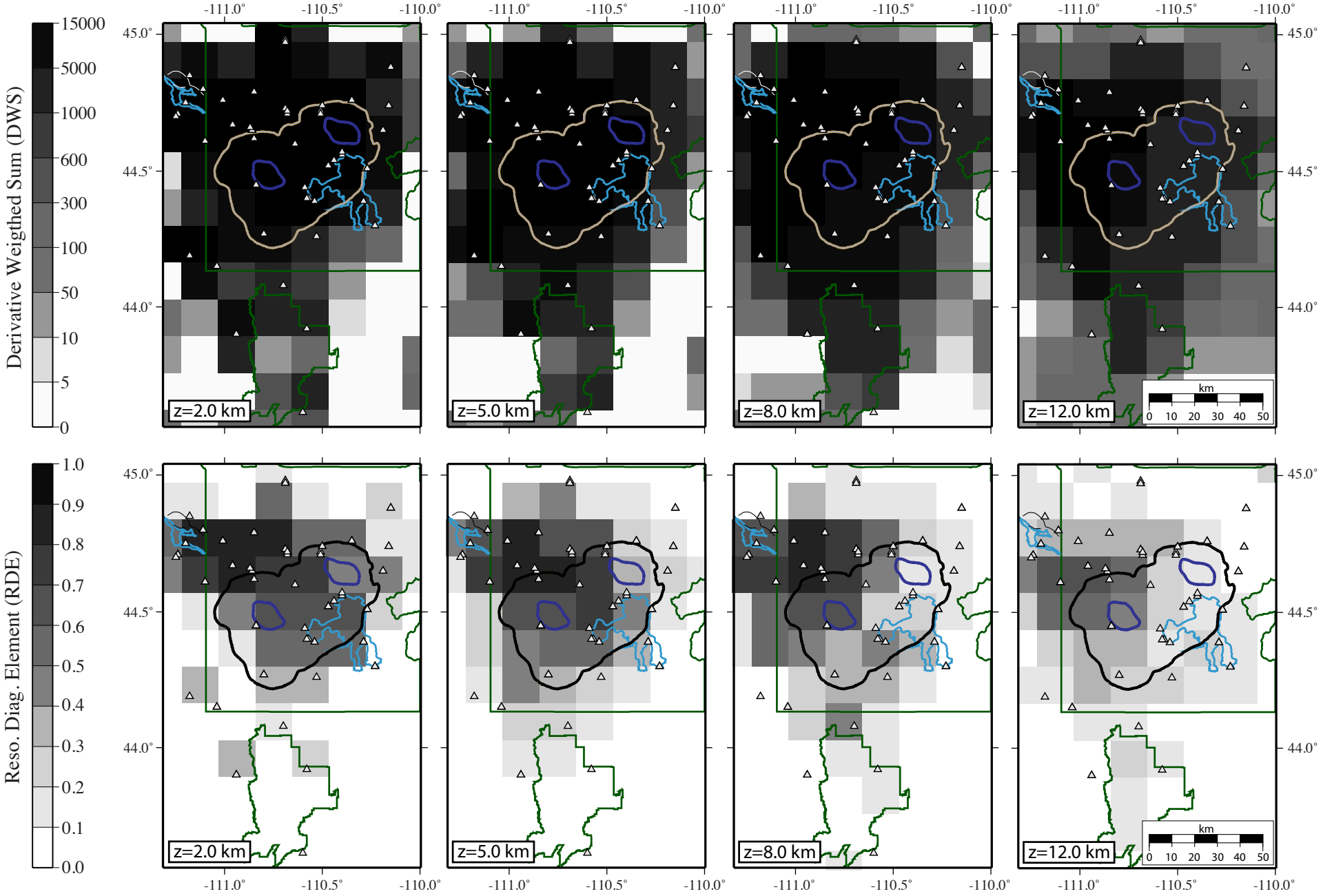
Derivative Weigthed Sum (DWS)
15000
5000
1000
600
300
100
50
10
5
0
Reso. Diag. Element (RDE)
1.0
0.9
0.8
0.7
0.6
0.5
0.4
0.3
0.2
0.1
0.0
-111.0°
-110.5°
-110.0°
45.0°
44.5°
44.0°
z=2.0 km
z=5.0 km
z=8.0 km
z=12.0 km
km
0 10 20 30 40 50

Fig. S04

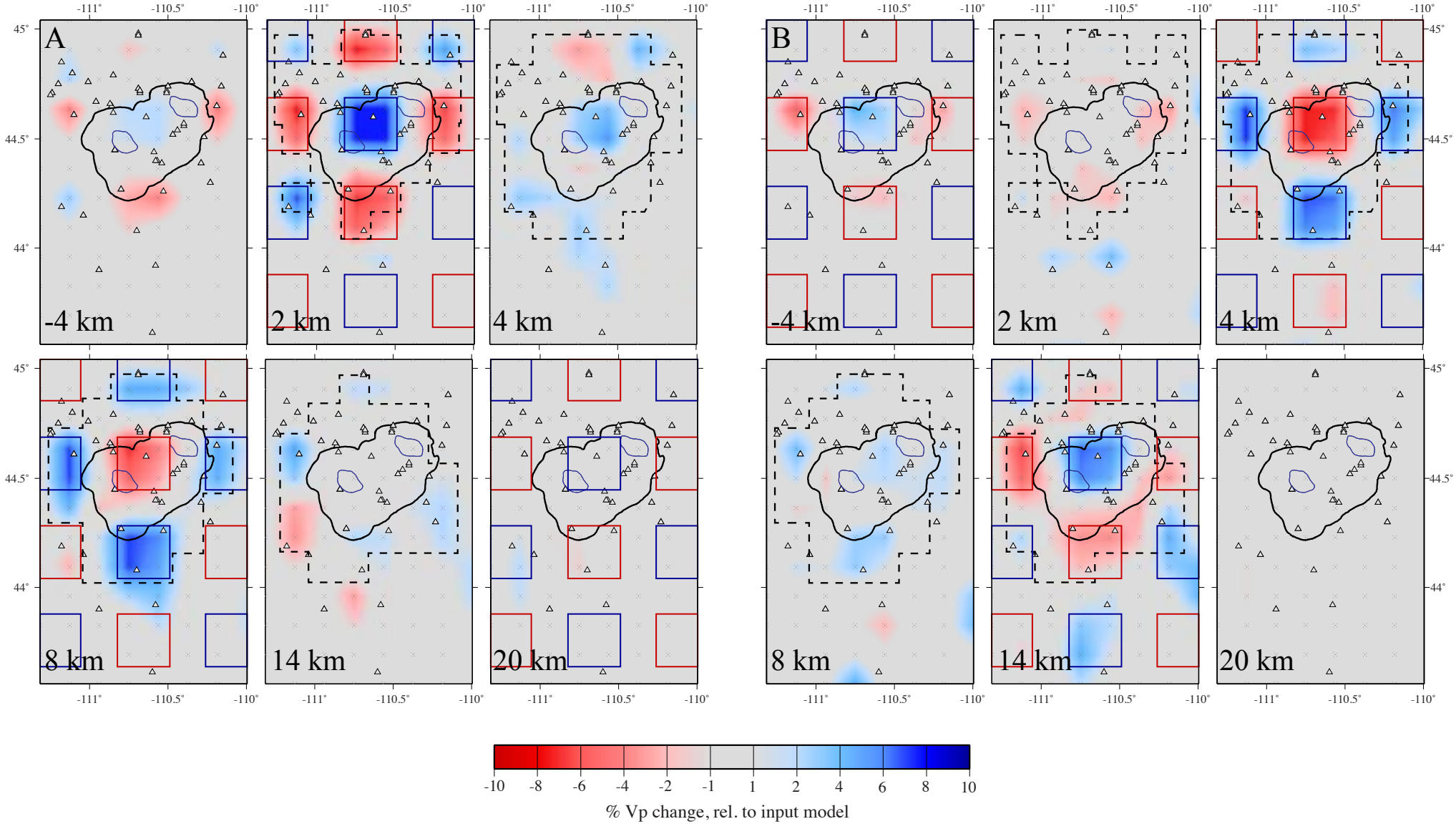
A
B
-4 km
2 km
4 km
8 km
14 km
20 km
-111°
-110.5°
-110°
45°
44.5°
44°
-10
-8
-6
-4
-2
-1
1
2
4
6
8
10
% Vp change, rel. to input model

Fig. S05

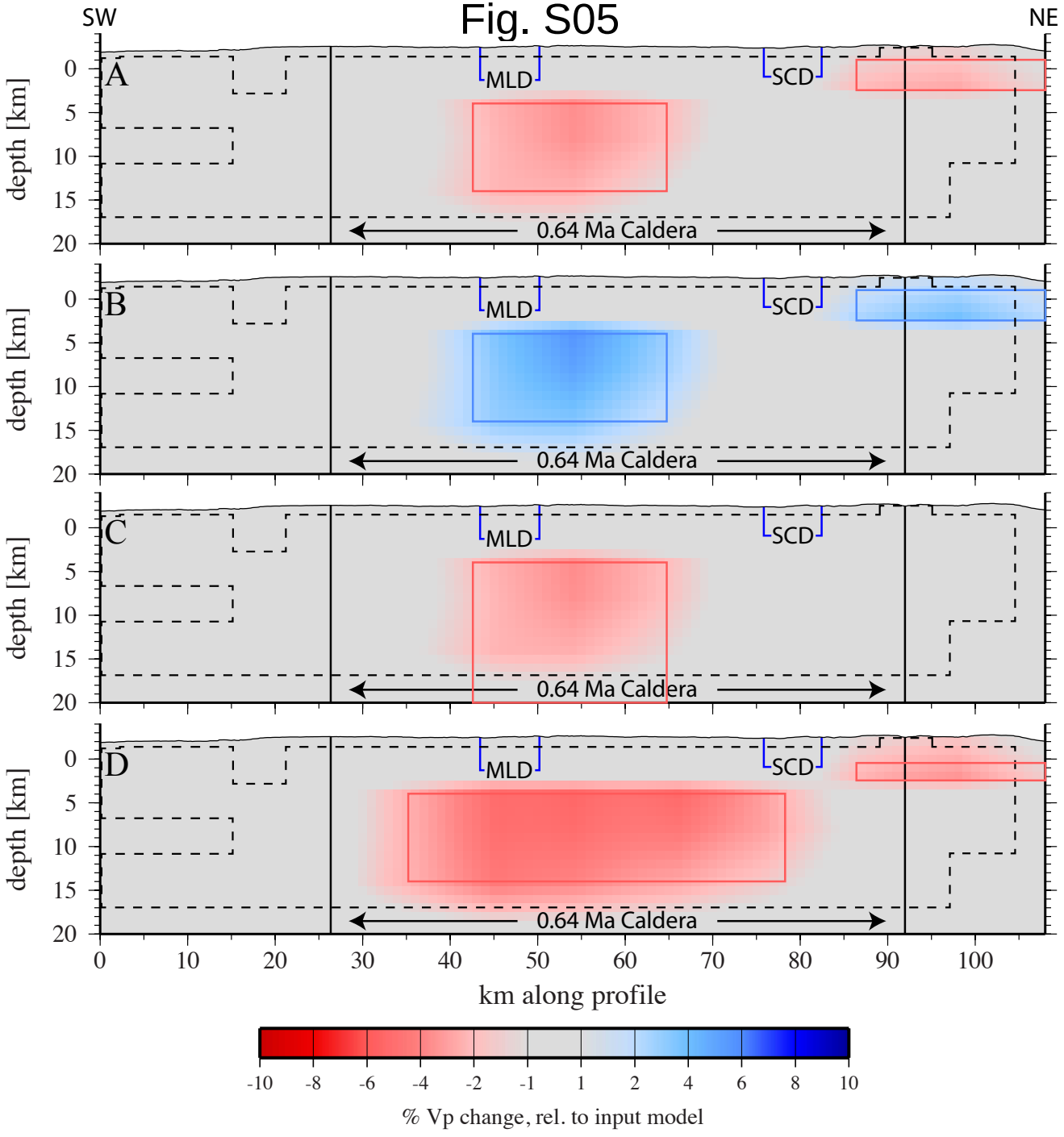
SW
NE
A
B
C
D
MLD
SCD
0.64 Ma Caldera
depth [km]
0
5
10
15
20
0
10
20
30
40
50
60
70
80
90
100
km along profile
-10
-8
-6
-4
-2
-1
1
2
4
6
8
10
% Vp change, rel. to input model

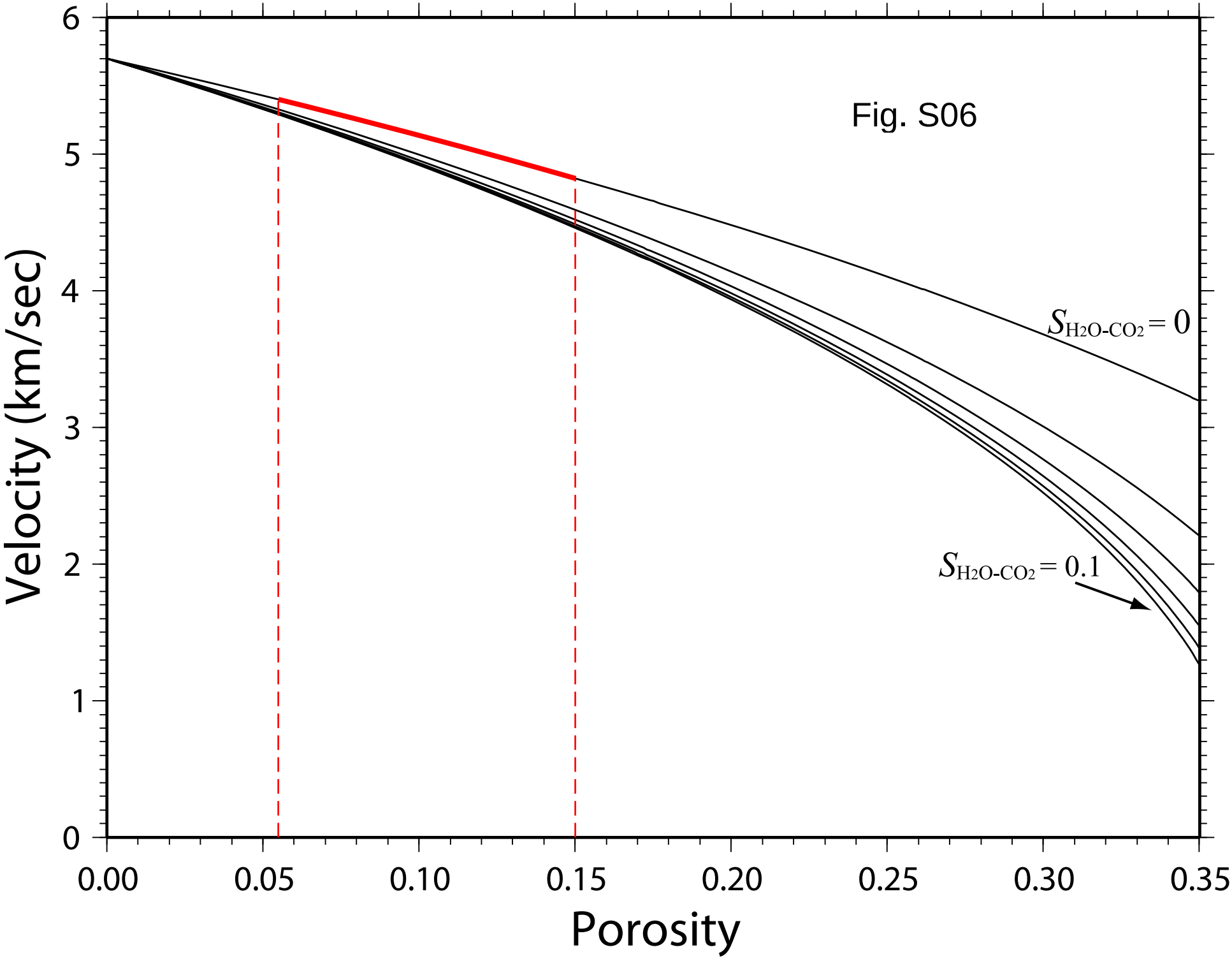
Fig. S06
Velocity (km/sec)
Porosity
0
1
2
3
4
5
6
0.00
0.05
0.10
0.15
0.20
0.25
0.30
0.35
$S_{H2O\text{-}CO2} = 0$
$S_{H2O\text{-}CO2} = 0.1$

Fig. S07

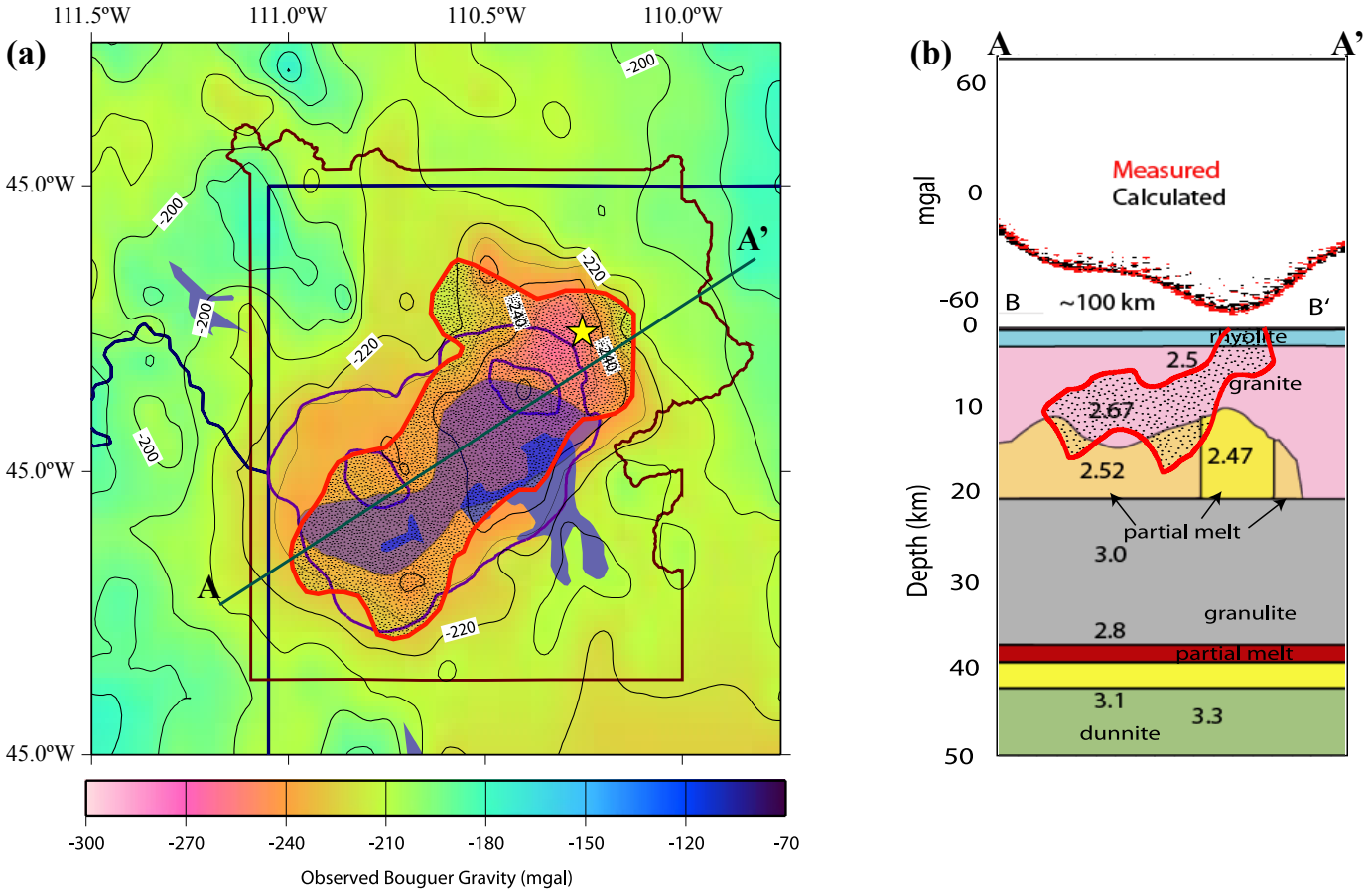
(a)
111.5°W
111.0°W
110.5°W
110.0°W
45.0°W
45.0°W
45.0°W
A
A'
-200
-220
-240
-300
-270
-240
-210
-180
-150
-120
-70
Observed Bouguer Gravity (mgal)
(b)
A
A'
60
0
-60
mgal
Measured
Calculated
B
~100 km
B'
0
10
20
30
40
50
Depth (km)
rhyolite
2.5
granite
2.67
2.47
2.52
partial melt
3.0
granulite
2.8
partial melt
3.1
3.3
dunnite

Fig. S08

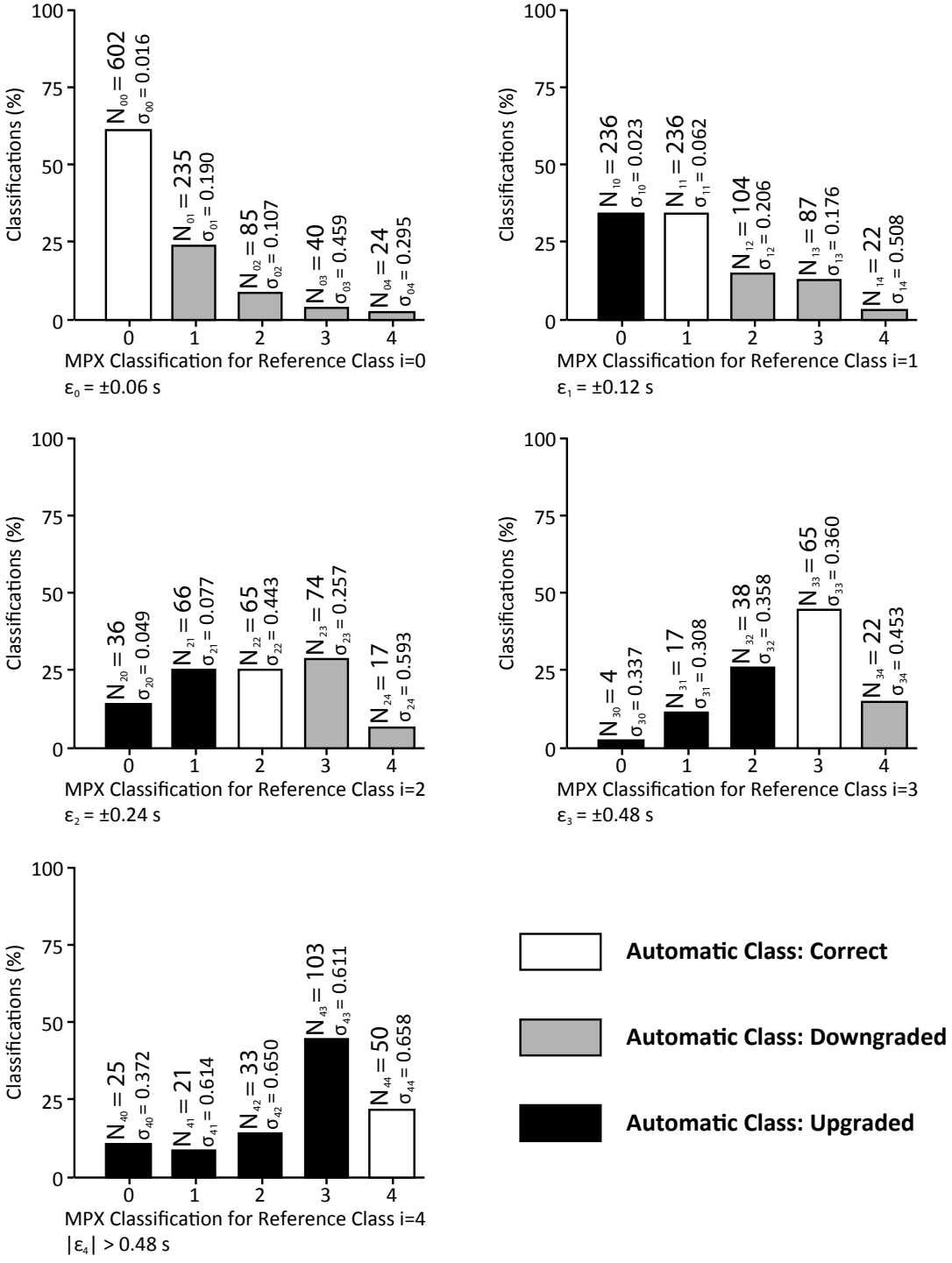
Classifications (%)
100
75
50
25
0
0
1
2
3
4
N00 = 602
σ00 = 0.016
N01 = 235
σ01 = 0.190
N02 = 85
σ02 = 0.107
N03 = 40
σ03 = 0.459
N04 = 24
σ04 = 0.295
MPX Classification for Reference Class i=0
ε0 = ±0.06 s
N10 = 236
σ10 = 0.023
N11 = 236
σ11 = 0.062
N12 = 104
σ12 = 0.206
N13 = 87
σ13 = 0.176
N14 = 22
σ14 = 0.508
MPX Classification for Reference Class i=1
ε1 = ±0.12 s
N20 = 36
σ20 = 0.049
N21 = 66
σ21 = 0.077
N22 = 65
σ22 = 0.443
N23 = 74
σ23 = 0.257
N24 = 17
σ24 = 0.593
MPX Classification for Reference Class i=2
ε2 = ±0.24 s
N30 = 4
σ30 = 0.337
N31 = 17
σ31 = 0.308
N32 = 38
σ32 = 0.358
N33 = 65
σ33 = 0.360
N34 = 22
σ34 = 0.453
MPX Classification for Reference Class i=3
ε3 = ±0.48 s
N40 = 25
σ40 = 0.372
N41 = 21
σ41 = 0.614
N42 = 33
σ42 = 0.650
N43 = 103
σ43 = 0.611
N44 = 50
σ44 = 0.658
MPX Classification for Reference Class i=4
|ε4| > 0.48 s
Automatic Class: Correct
Automatic Class: Downgraded
Automatic Class: Upgraded

Fig. S09

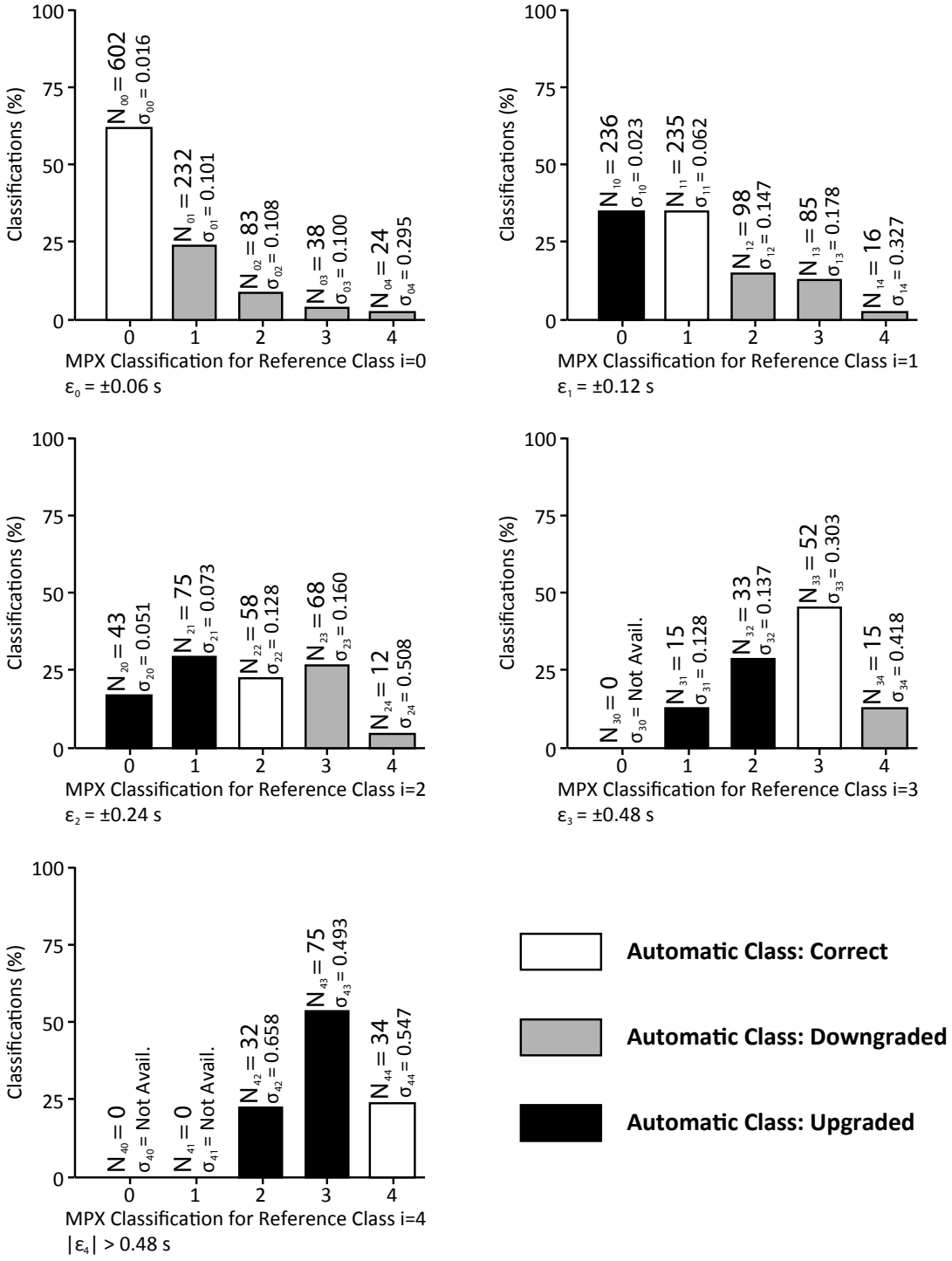
Classifications (%)
100
75
50
25
0
0
1
2
3
4
N00 = 602
σ00 = 0.016
N01 = 232
σ01 = 0.101
N02 = 83
σ02 = 0.108
N03 = 38
σ03 = 0.100
N04 = 24
σ04 = 0.295
MPX Classification for Reference Class i=0
ε0 = ±0.06 s
N10 = 236
σ10 = 0.023
N11 = 235
σ11 = 0.062
N12 = 98
σ12 = 0.147
N13 = 85
σ13 = 0.178
N14 = 16
σ14 = 0.327
MPX Classification for Reference Class i=1
ε1 = ±0.12 s
N20 = 43
σ20 = 0.051
N21 = 75
σ21 = 0.073
N22 = 58
σ22 = 0.128
N23 = 68
σ23 = 0.160
N24 = 12
σ24 = 0.508
MPX Classification for Reference Class i=2
ε2 = ±0.24 s
N30 = 0
σ30 = Not Avail.
N31 = 15
σ31 = 0.128
N32 = 33
σ32 = 0.137
N33 = 52
σ33 = 0.303
N34 = 15
σ34 = 0.418
MPX Classification for Reference Class i=3
ε3 = ±0.48 s
N40 = 0
σ40 = Not Avail.
N41 = 0
σ41 = Not Avail.
N42 = 32
σ42 = 0.658
N43 = 75
σ43 = 0.493
N44 = 34
σ44 = 0.547
MPX Classification for Reference Class i=4
|ε4| > 0.48 s
Automatic Class: Correct
Automatic Class: Downgraded
Automatic Class: Upgraded

Fig. S10

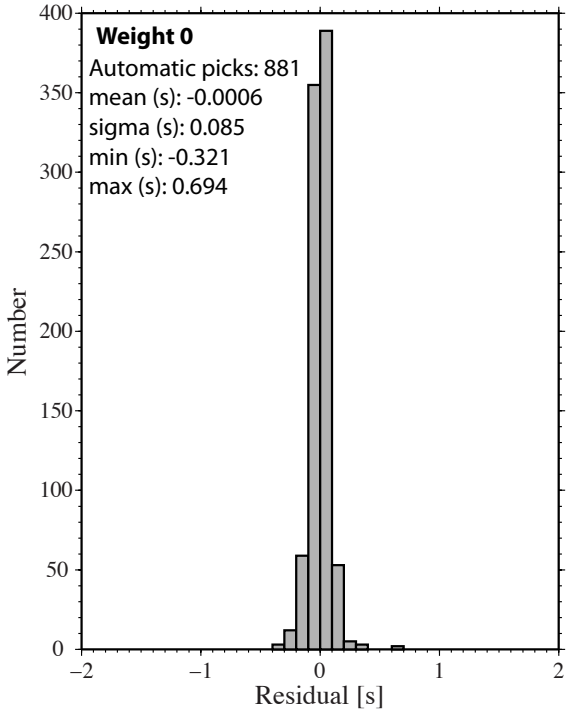

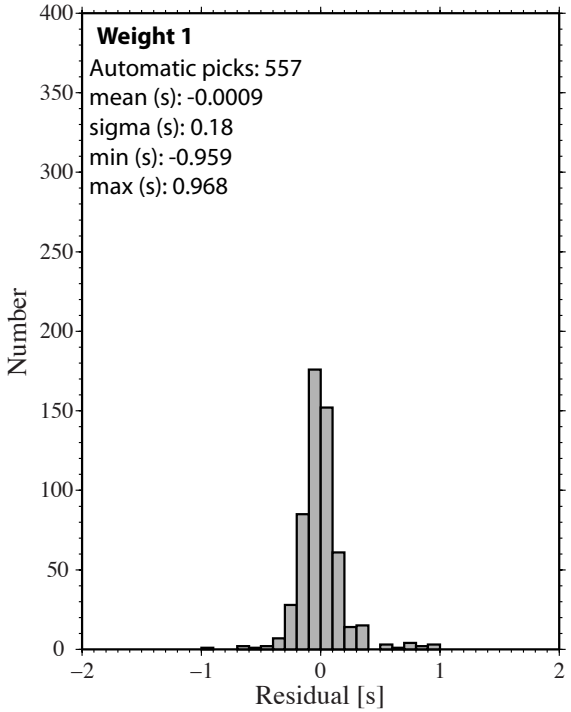

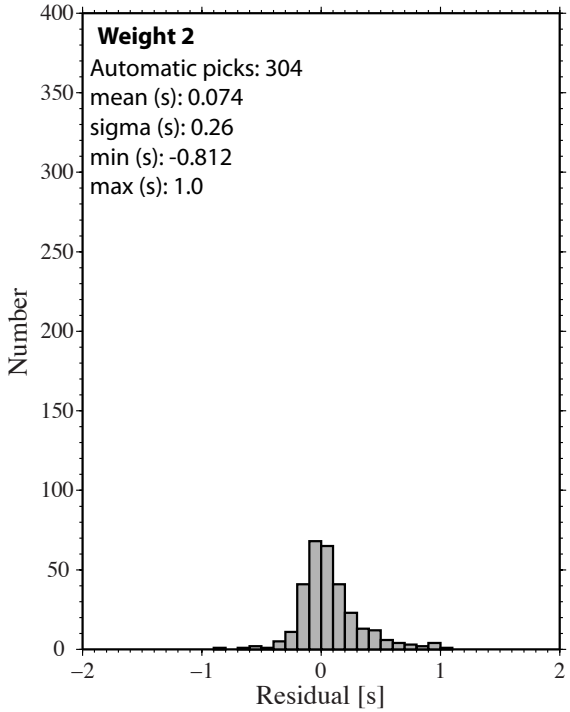

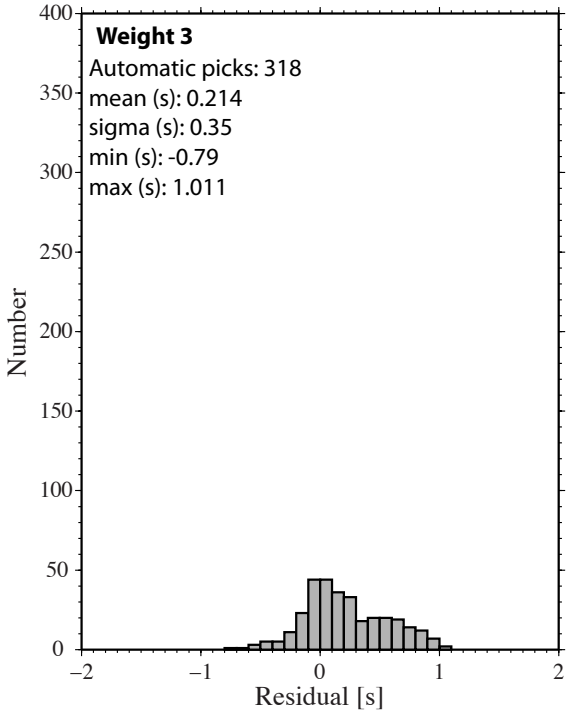

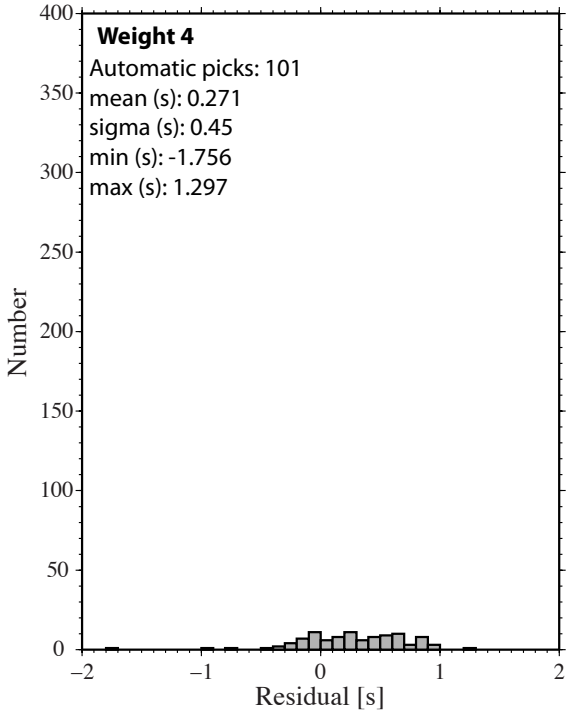

Weighting Scheme

Wt. 0 : 0.06 s
Wt. 1 : 0.12 s
Wt. 2 : 0.24 s
Wt. 3 : 0.48 s
Wt. 4 : > 0.48 s